Electronic Supplementary Material (ESI) for Nanoscale.
This journal is © The Royal Society of Chemistry 2016

Supplementary Informations

Hyperbranched polymer mediated size-controlled synthesis of gadolinium phosphate nanoparticles: colloidal properties and particle size-dependence on MRI relaxivity

Camille Frangville[a,‡], Maylis Gallois[a,‡], Yichen Li[b,‡], Hanh Hong Nguyen[a], Nancy Lauth-de Viguerie[a], Daniel Talham[b,*], Christophe Mingotaud[a] and Jean-Daniel Marty[a,*]

a Laboratoire des Interactions Moléculaires et Réactivités Chimiques et Photochimiques, Université de Toulouse, CNRS UMR 5623, 31062 Toulouse Cedex 09, France.

b Department of Chemistry, University of Florida, Gainesville, Florida 32611-7200, United States

Index

S1. POLYMER SYNTHESIS. 3

Figure S1A. Synthesis of HYPAM based hyperbranched polymers with a single or double shell. 3
Figure S1B. ^{1}H NMR 400 MHz of HYPAM in D_20 (bottom) and HYPAM-C_{18}-PEG in $CDCl_3$ in the region from 2 to 3 ppm. Although the intensity cannot be normalized, the spectra detail show the evident modification of the peak at 2.7 ppm attributed to the methylene in alpha of the primary amines in the HYPAM, after functionalization with the double shell. 4
Figure S1C. DSC thermograms for HyPAM, HyPAM-PEG and HyPAM-C_{18}-PEG at a heating rate of 10°C/min. 5

S2. ELECTRON DIFFRACTION PATTERNS AND LATTICE PARAMETERS 6

Figure S2.A. TEM picture of HyPAM-PEG $GdPO_4$ and corresponding electron diffraction pattern 6
Figure S2.B. X-ray diffraction diagram of $GdPO_4$ NPs and corresponding lattice parameters 6

S3. GD^{3+} / HYPAM ^{1}H NMR MEASUREMENTS 7

Figure S3. ^{1}H NMR study of Gd^{3+} / HyPAM interactions 7

S4. $GDPO_4$ / HYPAM, HYPAM-PEG, HYPAM-C_{18}-PEG - RELAXIVITY MEASUREMENTS 8

Figure S4.A. Relaxation rates ($1/T_1$, $1/T_2$) as a function of Gd^{3+} concentrations, for HyPAM / $GdPO_4$ lengths range (6nm – 118nm) 8
Figure S4.B. Relaxivity (r_1 ,r_2) as a function of HyPAM / $GdPO_4$ NPs lengths 9
Figure S4.C. Relaxation rates ($1/T_1$, $1/T_2$) comparison for HyPAM, HyPAM-PEG and HyPAM-C_{18}-PEG / $GdPO_4$ NPs 10

S5. $GDPO_4$ / HYPAM, HYPAM-PEG, HYPAM-C_{18}-PEG - SIZE-CONTROLLED SYNTHESIS 11

Figure S5.A. TEM pictures of $GdPO_4$ nanowires with HyPAM and functionalized HyPAMs. 11
Figure S5.B. $GdPO_4$ nanowires length versus polymers concentrations 11
Figure S5.C. Enlargement of TEM images of HyPAM coated $GdPO_4$ nanoparticles 12

S6. $GDPO_4$ / HYPAM, HYPAM-PEG, HYPAM-C_{18}-PEG – DLS STUDIES AND NACL ADDITION 13

Figure S6A. DLS correlogram and corresponding distribution. 13
HyPAM (without filtration as filtrated samples appeared with poor quality correlograms) 13
Figure S6B. DLS correlogram of $GdPO_4$/HyPAM and functionalized HyPAMs with NaCl 17

S7. $GDPO_4$ / HYPAM, HYPAM-PEG, HYPAM-C_{18}-PEG – DRUG LOADING CAPACITY 18

Figure S7. Fluorescence studies of Nile Red in $GdPO_4$/HyPAM and functionalized HyPAMs systems 18

S8. CELL VIABILITY OF CEM CELLS IN PRESENCE OF GDPO4/HYPAM-C_{18}-PEG NANOPARTICLES 19

S1. Polymer synthesis.

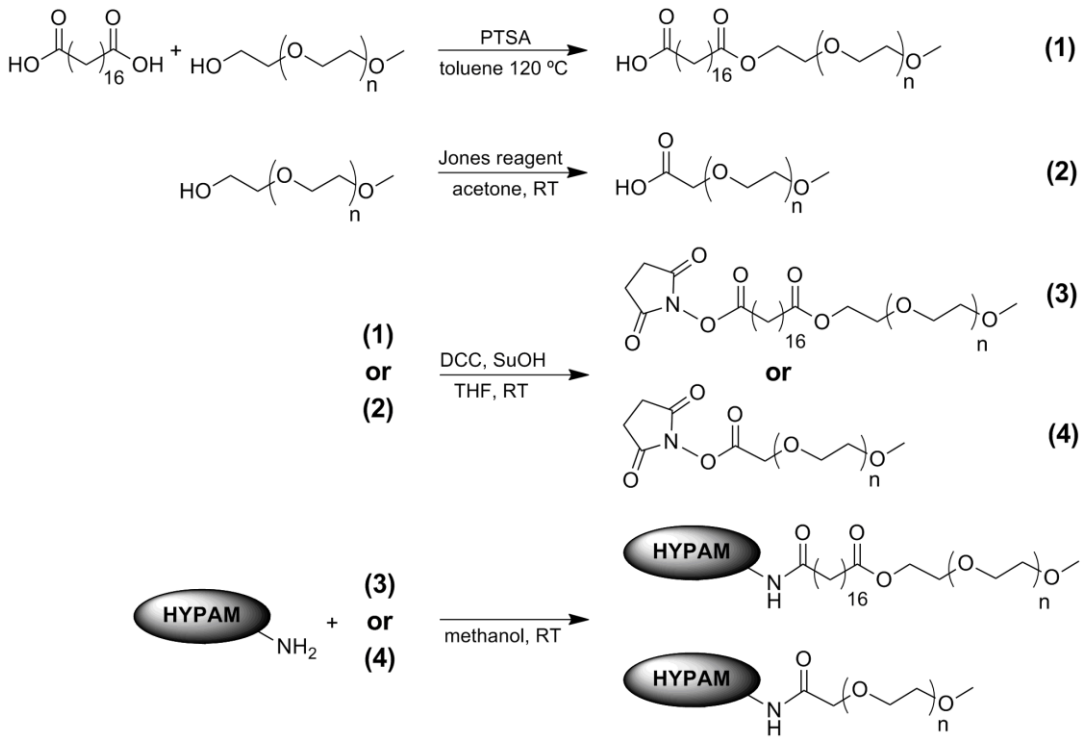

Figure S1A. Synthesis of HYPAM based hyperbranched polymers with a single or double shell.

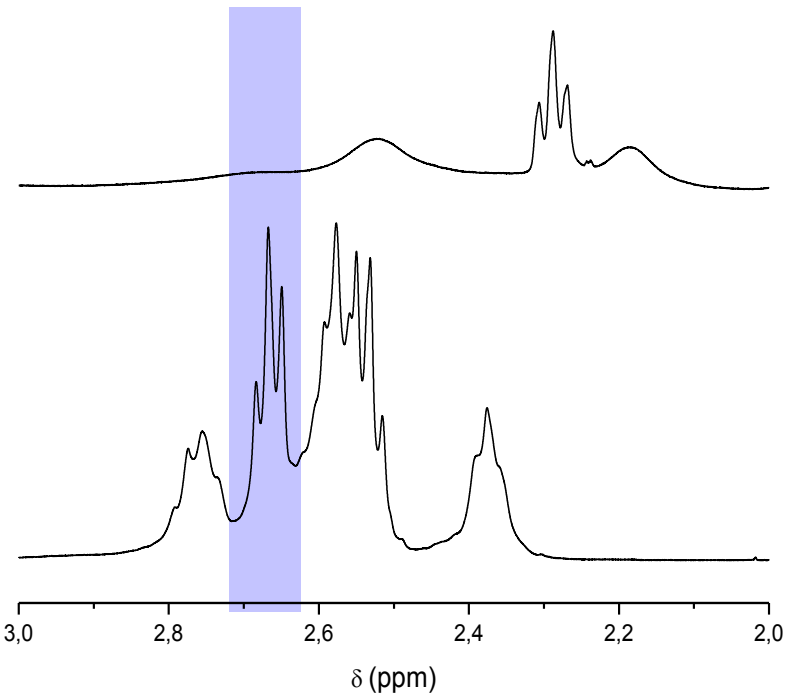

Figure S1B. ^{1}H NMR 400 MHz of HYPAM in D_20 (bottom) and HYPAM-C_{18}-PEG in $CDCl_3$ in the region from 2 to 3 ppm. Although the intensity cannot be normalized, the spectra detail show the evident modification of the peak at 2.7 ppm attributed to the methylene in alpha of the primary amines in the HYPAM, after functionalization with the double shell.

HYPAM: ^{1}H NMR (400 MHz, D_2O) δ: 2.34 (m, -CH_2-CO-); 2.5 (m, N-*CH_2*-*CH_2*-N); 2.55 (m, CONH-CH_2-*CH_2*-N); 2.63 (m, -*CH_2*-NH_2); 2.73 (m, N-*CH_2*-CH_2-CO); 3.22 (m, -*CH_2*-NHCO-) ppm. ^{1}H NMR (400 MHz, $CDCl_3$) δ (ppm): 2.1-2.9 (m, -*NH_2*, -*CH_2*-NH_2, -*CH_2*-CO-); 3.25 (br m, -*CH_2*-NHCO-); 8.29 (br s, -NHCO-).
^{13}C NMR (100 MHz, D_2O) δ: 32.6, 35.5 (-*CH_2*-CO); 36.7 (-*CH_2*-NH-CO-); 37.8 (-*CH_2*-NH_2); 49.1 (N-*CH_2*-CH_2-CO); 49.8, 51.1, 52.5 (CONH-CH_2-*CH_2*-N); 56.0 (N-*CH_2*-*CH_2*-N); 174.5 (*CONH*) ppm.

HYPAM-C_{18}-PEG: ^{1}H NMR (400MHz, $CDCl_3$) δ: 4.18 (t, -COO-*CH_2*); 3.82-3.40 (br , -O-*CH_2*-*CH_2*-O- from mPEG); 3.35 (s, -O-*CH_3*); 3.21 (br, -CO-NH-*CH_2*-); 2.69 (br, CO-NH-CH_2-*CH_2*-N- and NHCO-CH_2-*CH_2*-N- from HYPAM); 2.52 (br, -N-*CH_2*-*CH_2*-N- and -NH-*CH_2*-*CH_2*-NH- from HYPAM); 2.30 (t, -*CH_2*-COO-); 2.19 (br, NHCO*CH_2*); 1.58 (br, NHCO-CH_2-*CH_2*-$(CH_2)_{12}$-*CH_2*-CH_2-COO); 1.21 (m, NHCO-CH_2-CH_2-(*CH_2*)$_{12}$-CH_2-CH_2-COO-) ppm.
^{13}C NMR (100 MHz, $CDCl_3$) δ: 174.1 (-NH-*CO*-CH_2 from HYPAM core and core-shell link); 173.7 (-CH_2-*COO*-); 71.9 (-*CH_2*-O-CH_3); 70.5 (-O-*CH_2*-*CH_2*-O); 69.1 (-COO-CH_2-*CH_2*-); 63.3 (-COO-*CH_2*); 58.9 (-O-*CH_3*); 53.4 – 55.1 (N-*CH_2*-*CH_2*-N); 51.1-52.4 (CONH-CH_2-*CH_2*-N); 49.4-50.6 (N-*CH_2*-CH_2-CO); 37.6 (-CO-NH-*CH_2*-CH_2-N-); 36.4 (CO-NH-*CH_2*- from the core-shell link); 34.1 (NH-CO-*CH_2*); 28.8-30.9 (NHCO-CH_2-CH_2-(*CH_2*)$_{12}$-CH_2-CH_2-COO-); 25.9 (-NH-CO-CH_2-*CH_2*-); 24.8 (-*CH_2*-CH_2-COO-) ppm.

Determination of the degree of substitution of primary amines: degree of substitution was estimated from ^{1}H NMR spectra as follows:

- First, from the spectra of HYPAM, the sum of the intensity of the peaks at 3.25 and 2.7 ppm attributed to the methylene in alpha of the amide and amine function respectively was compared to the intensity of the peaks between 2.2 and 3.3 corresponding to all methylene groups in HYPAM. .
- Then on the HYPAM-C_{18}-PEG spectrum: the intensity of the peak at 3.21 ppm corresponding to the methylene in alpha of (-CO-NH-*CH_2*-) groups (including now the new substituted primary amine groups) was compared to the intensity of peaks between 2.2 and 3.3 corresponding to all methylene groups in HYPAM. This ratio is expected to be the same than the previous one if all primary amino groups were substituted.
- Any difference observed between the two previous ratio is thus directly related to the non-substituted primary amino groups and enable to calculate the substitution degree. Nevertheless, it has to be noted that only a rough estimation of substitution degree was obtained due to the width of the peaks.

Table S1. Properties of investigated polymers

	$\overline{M_w}$ [a]	Đ [b]	Thermal properties[c]	
			T_g (°C)	T_f (°C)
HyPAM	13000	1.4	-9.0 (0.5)	/
HyPAM-PEG	54000	1.5	/	23.4 (33)
HyPAM-C_{18}-PEG	69000	1.5	/	44.8 (82)

a Molecular weight determined by LS-SEC.
b Dispersity index determined by SEC.
c Thermal properties obtained from DSC measurements. Glass transition temperatures T_g were given at a heating rate of 10°C/min and fusion temperatures T_f were obtained from maximum peak values extrapolated at 0°C/min. n.r. not reported due to aggregation phenomenon.
d determined by using the measured molecular weight of HYPAM from SEC assuming an equivalent grafting ratio than the one observed with HYPAM-PEG

Differential scanning calorimetry (DSC) analyses were performed for all polymers. Figure S1B shows the thermograms obtained for $HyPAM_4$, $HyPAM_4$-PEG_{750} and $HyPAM_4$-C_{18}-PEG_{750}. They showed a transition temperature at around -9.0 °C for $HYPAM_4$ polymer that could be attributed to a glass transition temperature. This transition was no more visible when the HyPAM core was grafted with a single or a double shell. Instead an endothermic peak (with increasing associated enthalpy variation) appears at 23.4 and 44.8°C for HyPAM-PEG and HyPAM-C_{18}-PEG, respectively. Therefore in bulk, these polymers tend to organize at a molecular level. As this process was greatly enhanced by the presence of the hydrophobic shell, this suggests the existence of alkyl/alkyl or PEG/PEG interactions.

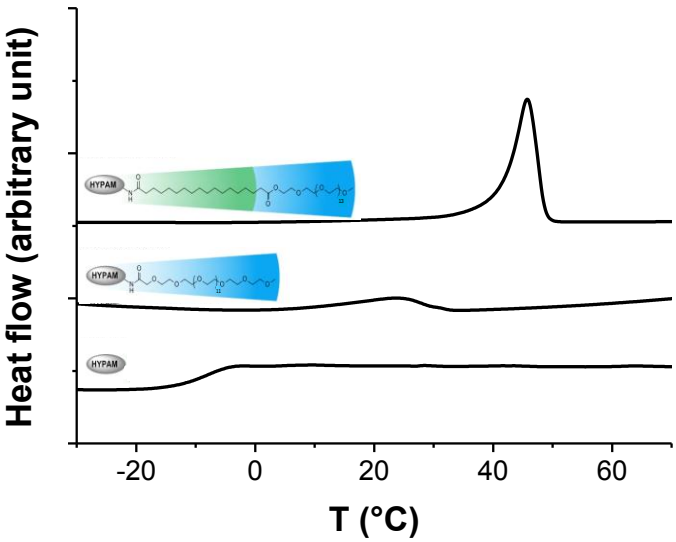

Figure S1C. DSC thermograms for HyPAM, HyPAM-PEG and HyPAM-C_{18}-PEG at a heating rate of 10°C/min.

S2. Electron diffraction patterns and lattice parameters

Selected Area Electron Diffraction (SAED) were performed to a. confirm the synthesis of $GdPO_4$ NPs through this polymer-based protocol and b. reject the presence or formation of Gadolinium oxides and hydroxides NPs (Gd_2O_3, and $Gd(OH)_3$.

Figure S2.A. TEM picture of HyPAM-PEG $GdPO_4$ and corresponding electron diffraction pattern

a. **b.**

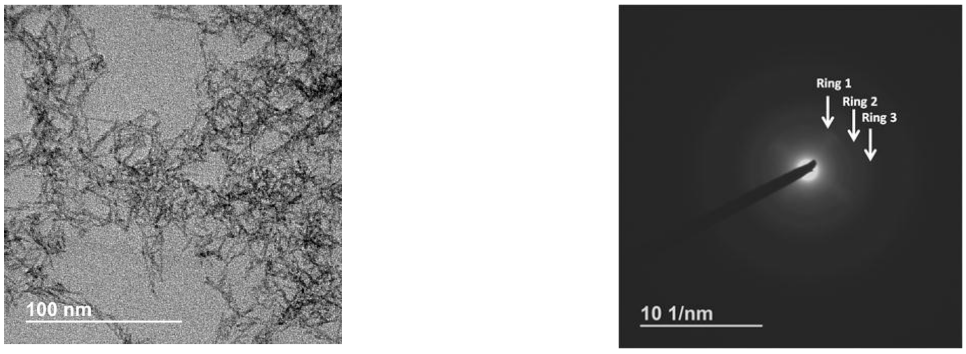

Figure S2A. a. TEM pictures HyPAM-PEG $GdPO_4$ NPs, b. corresponding electron diffraction pattern and selected analysis areas.

Figure S2.B. X-ray diffraction diagram of $GdPO_4$ NPs and corresponding lattice parameters

a.

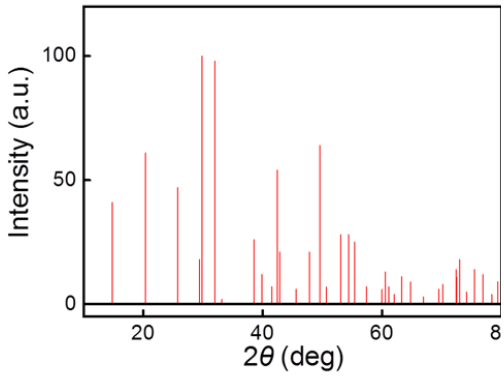

b.

	2 θ	(hkl)	Intensity	Reported d-spacing (Å)	Calculate d-spacing (
Ring 1	29.85 31.99	(2 0 0) (1 0 2)	100 98	2.991 2.795	2.861±0.0
Ring 2	42.44 42.84	(2 1 1) (0 03)	54 21	2.128 2.109	2.118±0.0
Ring 3	47.81 49.53	(3 0 1) (2 1 2)	21 64	1.901 1.839	1.865±0.0

c.

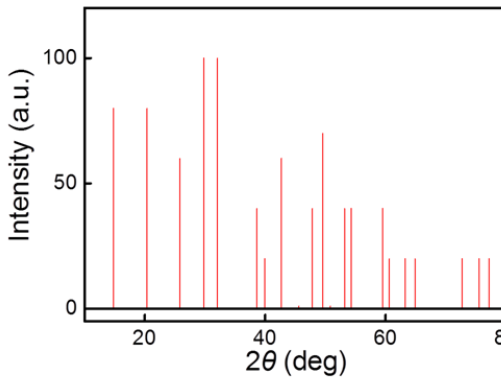

d.

	2 θ	(hkl)	Intensity	Reported d-spacing (Å)	Calculate d-spacing (
Ring 1	29.84 32.10	(2 0 0) (1 0 2)	100 100	2.992 2.786	2.861±0.01
Ring 2	42.70	(0 03)	60	2.116	2.118±0.02
Ring 3	47.86 49.58	(3 0 1) (2 1 2)	40 70	1.899 1.837	1.865±0.01

Figure S2B. a. (resp. c.) JCPDS file n°39-232 (resp. n°21-337) of $GdPO_4{\cdot}H_2O$ (resp. $GdPO_4{\cdot}1.5H_2O$), b. (resp. d.) comparison between the experimentally obtained X-ray diffraction spacing and the values reported in JCPDS.

These two experimental lattice parameters suggest the formation of $GdPO_4{\cdot}xH_2O$ with a non-defined extent of hydratation.

S3. Gd^{3+} / HyPAM ^1H NMR measurements

Interactions between HyPAM and Gd^{3+} ions were examined by ^1H NMR analysis. Increasing amounts of Gd^{3+} were introduced on HyPAM solution at a constant concentration (10^{-4}M) in D_20, pH were adjusted at 8-9.

Figure S3. ^1H NMR study of Gd^{3+} / HyPAM interactions

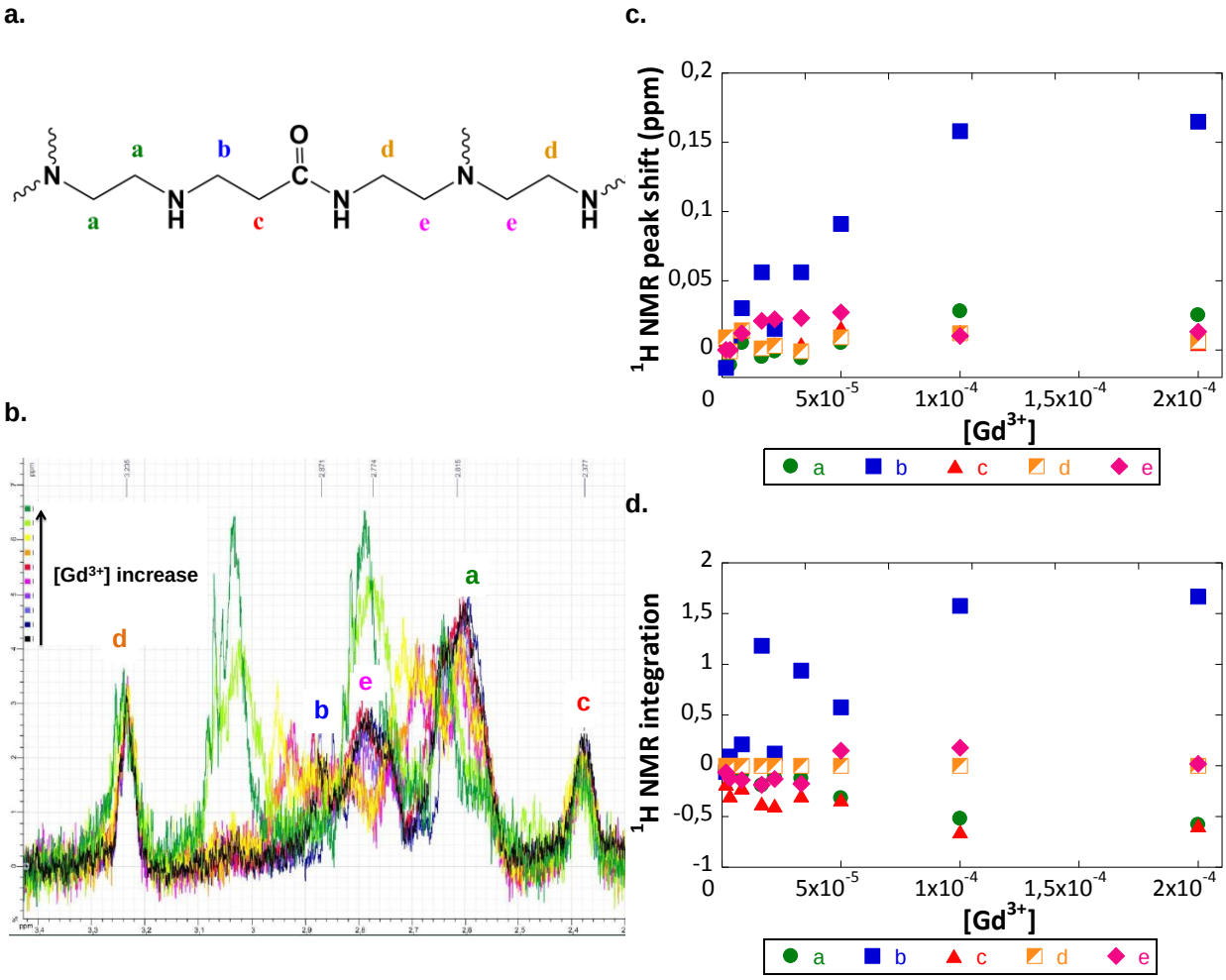

Figure S3A. ^1H NMR study for [HyPAM]=1.10^{-4}M and increasing amount of Gd^{3+} ions in D_2O; a. HyPAM protons classifications, b. ^1H NMR spectra, c. ^1H NMR peak shifts, d. ^1H NMR peak integrations with H_d protons set as reference.

As a result, only ^1H_b HyPAM protons peaks were found shifting and widening with the increase of Gd^{3+} ions compared to other protons (see Figure S2c.d.). These results highlight preferred interactions of Gd^{3+} with ^1H_b HyPAM protons located near tertiary amines.

S4. $GdPO_4$ / HyPAM, HyPAM-PEG, HyPAM-C_{18}-PEG - Relaxivity measurements

Transversal and longitudinal relaxation times T_1 and T_2 were recorded to assess the size dependence on their values along the range of $GdPO_4$ NPs synthesized with HyPAM.

Figure S4.A. Relaxation rates ($1/T_1$, $1/T_2$) as a function of Gd^{3+} concentrations, for HyPAM / $GdPO_4$ lengths range (6nm – 118nm)

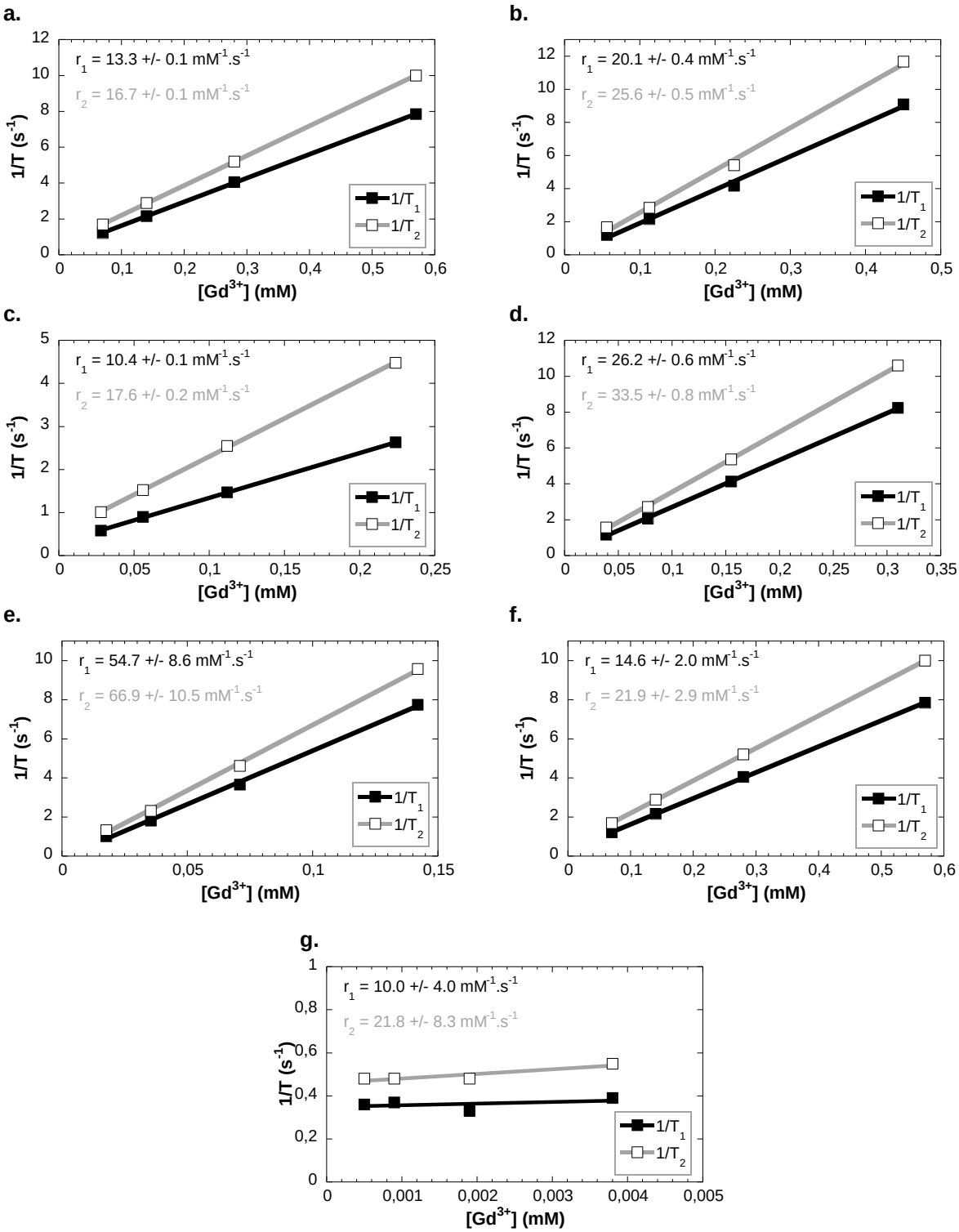

Figure S4A. Relaxation rates ($1/T_1$, $1/T_2$) as a function of [Gd^{3+}] for $GdPO_4$ NPs lengths : a. 6nm, b. 8nm, c. 12nm, d. 15nm, e. 23 nm, f. 32 nm, g. 118nm. (field 1.4 T, [HyPAM]=0-8 $\mu mol.L^{-1}$)

Relaxivity r_1 and r_2 are then assessed and plotted as a function of $GdPO_4$ NPs lengths.

Figure S4.B. Relaxivity (r_1 ,r_2) as a function of HyPAM / $GdPO_4$ NPs lengths

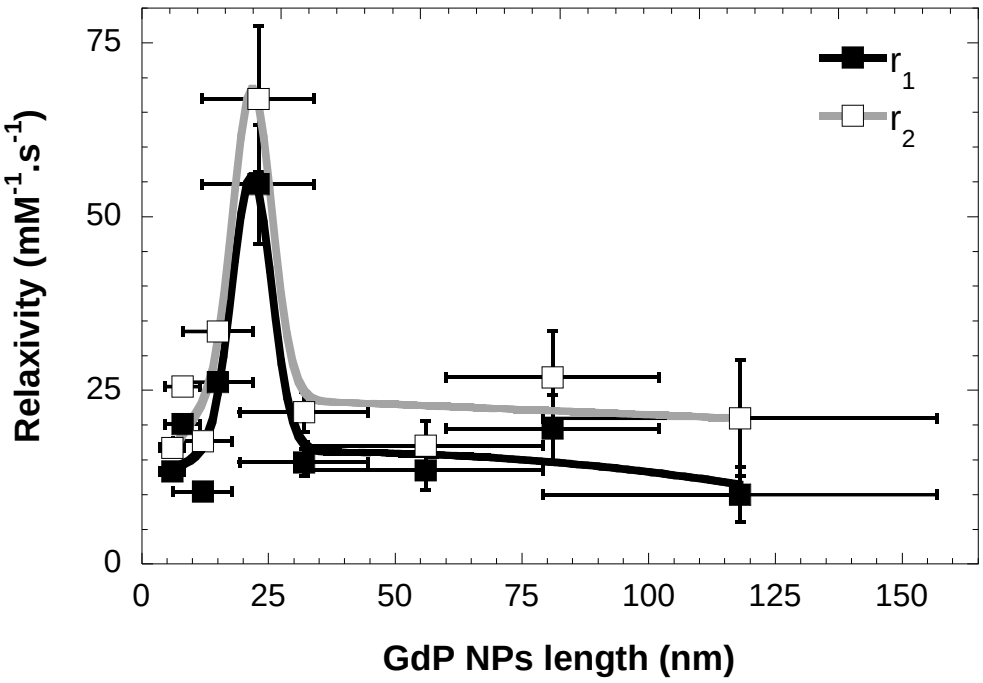

Figure S4B. Relaxivities (r_1 and r_2 as a function of $GdPO_4$ NPs length. (field 1.4 T).

The particle size dependence on r_1 and r_2 shows an optimum size for the 23 nm particle sample were r_1 = 55±9 $mM^{-1}.s^{-1}$ and r_2 = 67±11 $mM^{-1}.s^{-1}$ were obtained. Lower values of relaxivity were collected for both larger and smaller particles.
Lastly, r_1 and r_2 relaxivity measurements were performed for the $GdPO_4$ nanoparticles stabilized with the PEG-containing hyperbranched polymers. Comparison of their relaxation rates are display below.

Figure S4.C. Relaxation rates ($1/T_1$, $1/T_2$) comparison for HyPAM, HyPAM-PEG and HyPAM-C_{18}-PEG / $GdPO_4$ NPs

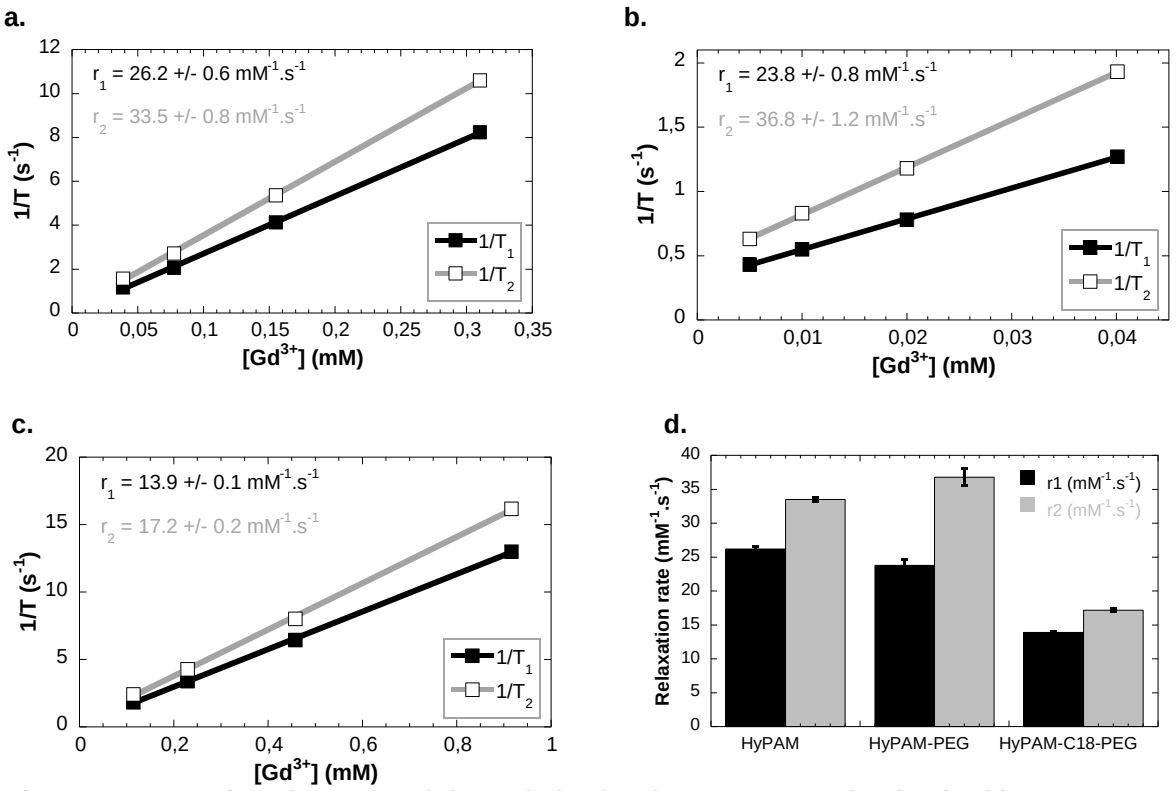

Figure S4C. Relaxation rates ($1/T_1$, $1/T_2$) of $GdPO_4$ NPs synthesized with a. HyPAM, b. HyPAM-PEG, c. HyPAM-C_{18}-PEG, d. relaxivities (r_1, r_2) comparison. (field 1.4 T, [Polymer]=5 µmol.L^{-1}).

As a result, $GdPO_4$ NPs synthesized with HyPAM or HyPAM-PEG exhibit similar relaxivity values whereas $GdPO_4$ NPs synthesized with HyPAM-C18-PEG display lower relaxivity values.

S5. $GdPO_4$ / HyPAM, HyPAM-PEG, HyPAM-C_{18}-PEG - Size-controlled synthesis

HyPAM and functionalized core-shell(s) concentration dependence on $GdPO_4$ nanowires was studied for constant concentrations of Gd^{3+} and PO_4^{3-} (10^{-4}M) and increasing amount of polymers (from 0 to 8 µM).

Figure S5.A. TEM pictures of $GdPO_4$ nanowires with HyPAM and functionalized HyPAMs.

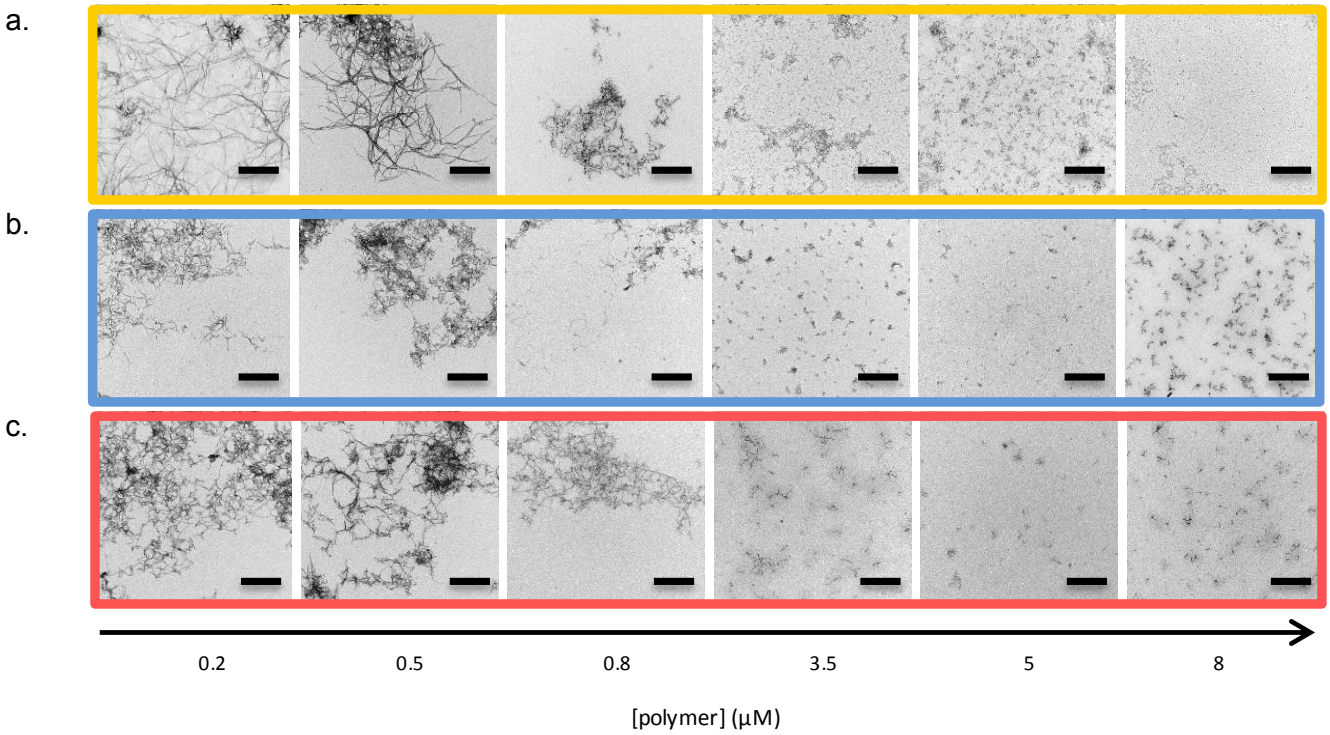

Figure S5A.TEM pictures of $GdPO_4$ nanowires synthesized with increasing amount of a. HyPAM, b. HyPAM-PEG, c. HyPAM-C_{18}-PEG, scale bars = 200nm.

Figure S5.B. $GdPO_4$ nanowires length versus polymers concentrations

a.

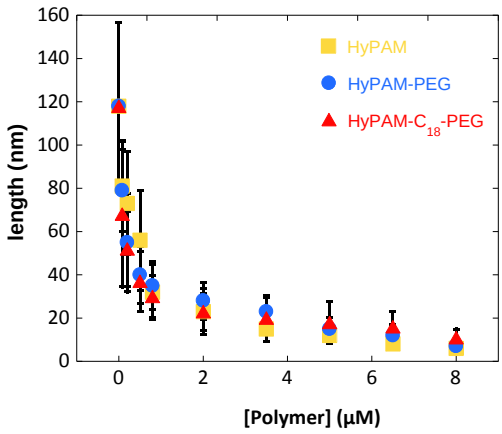

b.

	Nanowires length (nm)		
Polymer (µM)	HyPAM	HyPAM-PEG	HyPAM-C_{18}-PEG
0	118 ±39	118 ±39	118 ±39
0.08	81 ±21	79 ±19	68 ±34
0.2	73 ±23	55 ±23	52 ±17
0.5	56 ±23	40 ±13	37 ±14
0.8	32 ±13	35 ±11	30 ±10
2	23 ±9	28 ±9	23 ±11
3.5	15 ±0.6	23 ±7	20 ±11
5	12 ±0.1	15 ±5	18 ±10
6.5	8 ±0.4	12 ±5	16 ±7
8	6 ±0.1	7 ±3	11 ±4

Figure S5B. TEM-corresponding lengths of $GdPO_4$ nanowires; a. length (nm) versus polymer concentrations, b. recapitulative table with standard deviation.

As a result, $GdPO_4$ nanowires lengths were found dependent on polymer concentrations. They possess the same behavior for each type of hyperbranched polymers studied.

Figure S5.C. Enlargement of TEM images of HyPAM coated $GdPO_4$ nanoparticles

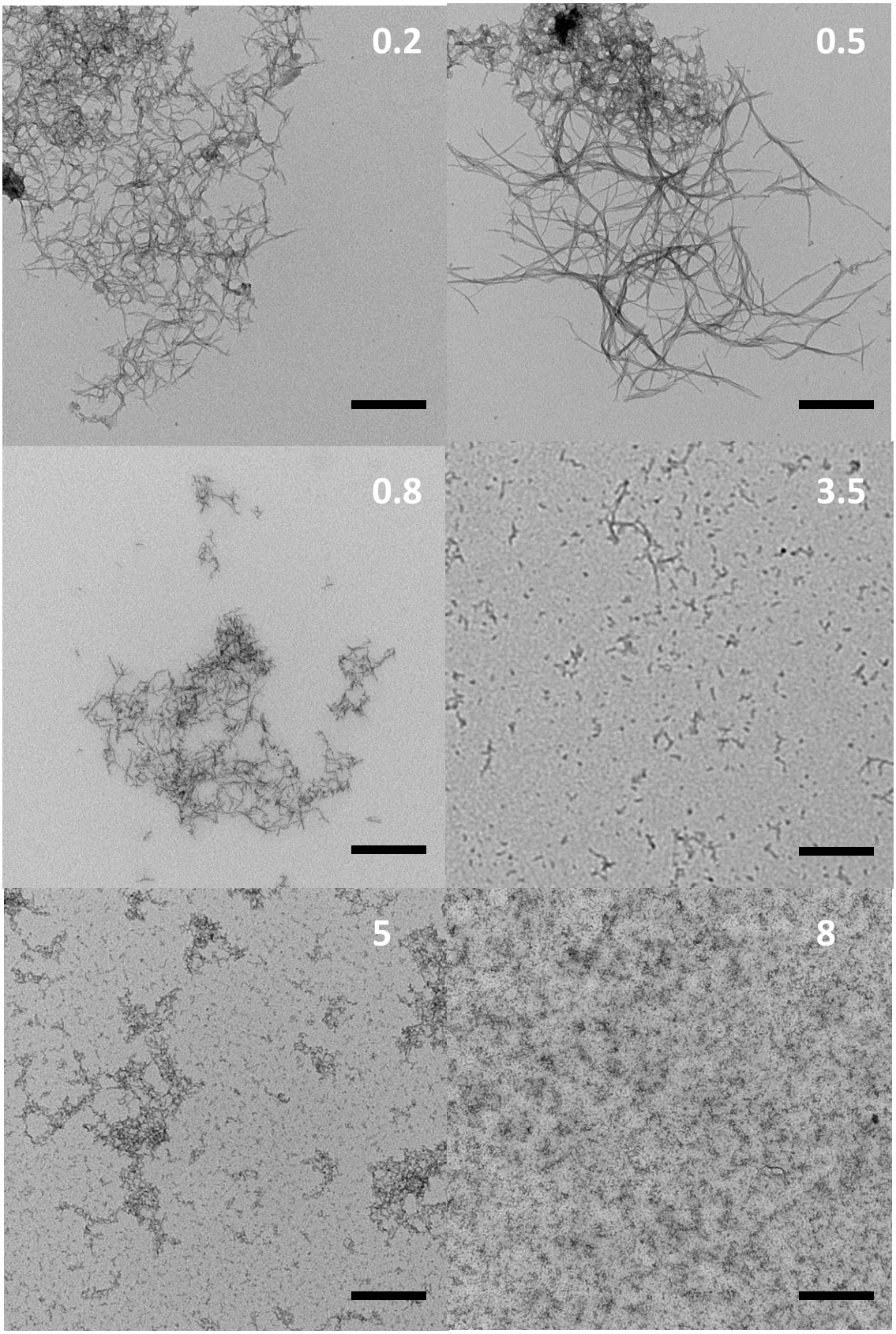

Figure S5C. Enlargement of TEM images of $GdPO_4$ nanoparticles synthesized with increasing amounts of HyPAM ($[Na_2HPO_4]_i$=5.10^{-4} mol.L^{-1}; $[Gd(NO_3)_3]$= 5.10^{-4} mol.L^{-1}; [HyPAM]=0 to 8 µmol.L^{-1} ; $pH_{adjusted}$ = 8-9) , before dialysis, scale bars = 200nm.

S6. $GdPO_4$ / HyPAM, HyPAM-PEG, HyPAM-C_{18}-PEG – DLS studies and NaCl addition

To control the input of functionalized core-shell(s) HyPAM, $GdPO_4$ nanowires synthesized with core and functionalized core-shell(s) polymers were evaluated towards NaCl addition (0.01 M, 0.1 M, 1 M)

Figure S6A. DLS correlogram and corresponding distribution.

HyPAM (without filtration as filtrated samples appeared with poor quality correlograms)

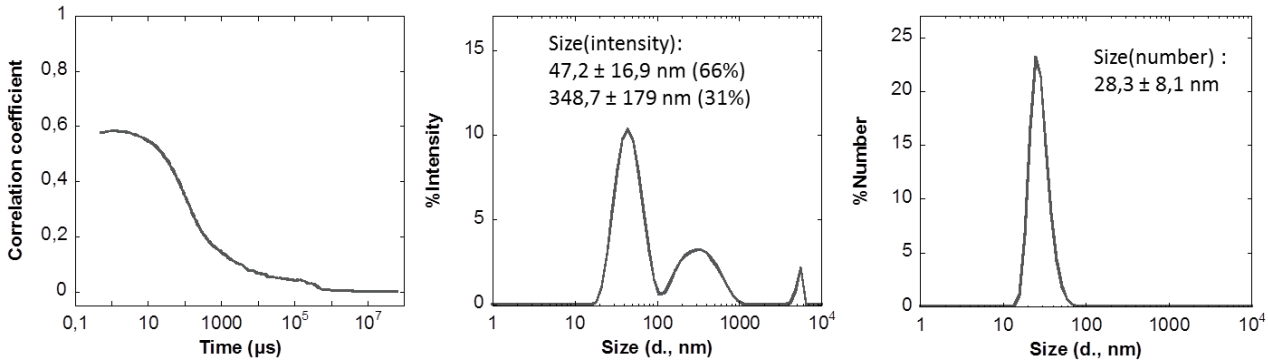

HyPAM-Peg and HyPAM-C_{18}-PEG (after filtration)

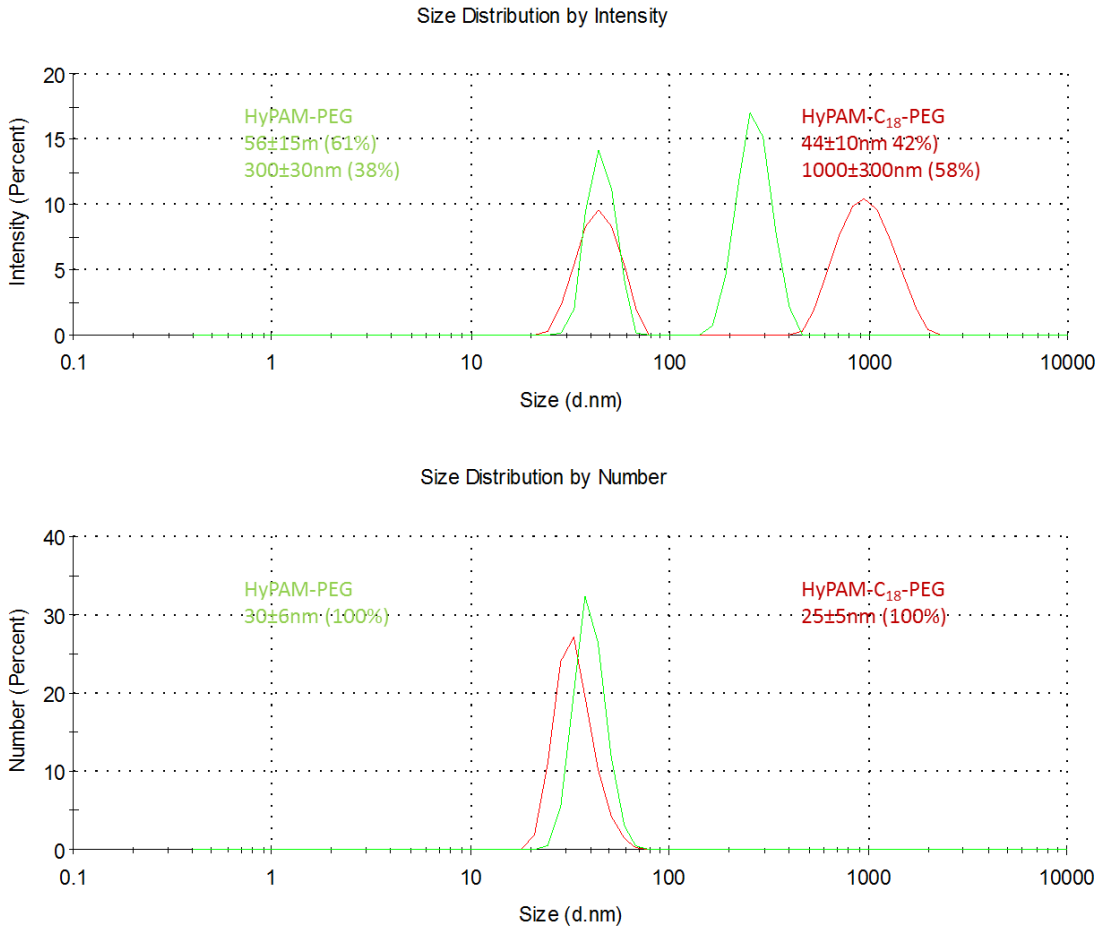

Figure S6A. DLS correlogram and corresponding apparent hydrodynamic diameter (in intensity and number) for HYPAM coated $GdPO_4$ NPs with [polymer]= 5 µmol.L^{-1}.

Theoretical background of Dynamic Light scattering (DLS).

DLS analysis was used to extract Z-average values, derived count rate, intensity and number average distributions for each studied nano-object sample. In order to give a critical view on the results issued from these analyses, a brief overview of the assumptions relative to these is given below.

From auto-correlation function to self-diffusion coefficient D. Particles in suspension (without sedimentation or creaming) undergo random Brownian motion with a characteristic (translational) diffusion coefficient D, which is related to the size and shape of the objects (see below). Under laser illumination, this motion induces a random fluctuation of the light scattered by the particles. The temporal behavior of the intensity of the scattered light contains therefore information on the particles' size and shape. To extract this information, analysis through auto-correlation of the scattered intensity signal could be performed. The auto-correlation intensity function $G(\tau,q)$ is defined as followed :

$$G(\tau,q) = \langle I(t,q).I(t+\tau,q)\rangle / \langle I(t,q)\rangle^2 \quad \textbf{(1)}$$

with <> denotes the integral of the function versus the time t
τ the delay time,
q the scattering vector $q = 4\pi\, n/\lambda_o \sin(\theta/2)$ with λ_o the incident laser wavelength, θ the scattering angle and n the optical index of the solution.

In the following parts, we suppose that each photon is scattered only once before being detected i.e. the solutions are diluted enough. When multiple scattering occurs, the results below are no longer correct.

In the case of *monodisperse and non-interacting nanoparticles,* $G(\tau,q)$ is following a single exponential decay:

$$G(\tau,q) = A.(1+\beta.[e^{-\Gamma.\tau}]^2) \quad \textbf{(2)}$$

with A the measured baseline,
β a parameter depending on the coherence optics,
Γ is a decay rate, which is equal to $q^2.D$.

Fitting the auto-correlation function of the experimental scattered intensity leads therefore to an estimation of the diffusion coefficient. Then, the size of the particle may be estimated from D after making assumption on the shape of the object. In the simple case of spherical particles, one will use the Stokes-Einstein equation:

$$R_h = k_B T/(6\pi\eta D) \text{ (Stokes Einstein)} \quad \textbf{(3)}$$

with R_h the hydrodynamic radius,
η the viscosity of the solution at the temperature T,
k_B the Boltzmann constant.

Note that the hydrodynamic radius is influenced by any changes of the nanoparticles surface structure or concentration of ions in the medium and that any mistake on the used viscosity and optical index values induces an important error on the calculated R_h. For anisotropic objects, the single exponential decay of the auto-correlation function is still observed for not so long objects (typically less than 150 nm). For such particles, various models have been developed to estimate a geometrical parameter of the particles (generally the length assuming a particular thickness over length ratio) from the translational diffusion (see JACS 2006, 128(5), 1639 and J Chem. Phys. 2003, 119, 8, 9914 for nanorods, Macromolecules 1979, 12(2), 320 for wormlike micelles, J. Chem. Phys. 2004, 121 (18), p 9111 for ellipsoids…). For longer objects, the auto-correlation functions are no more a single exponential decay and are influenced by both the translational and rotational diffusion coefficients (J. Chem. Phys. 1968, 48, 4126, Langmuir 2000, 16, 1689). Finally, whatever the geometry of the nanoparticles may be, the diffusion coefficient is affected by the concentration of particles, i.e. by the interparticle interactions. In the simplest form, the measured diffusion coefficient will follow (J. Phys. Chem. B, 2004, 108, 7021):

$$D = D_o.(1+k.\Phi_{eff}) \quad \textbf{(4)}$$

with D_0 the hydrodynamic radius without interparticle interactions,
k a constant, equal to 1.56 in the case of monodisperse hard spheres,
Φ_{eff} the effective volume fraction of particles.

Furthermore, the normalized average quantity of photon reaching the correlator (**Derived count rate** in the Malvern software) is a valuable indication to avoid misinterpretation issued from the single analysis of auto-correlation function. A low value for this quantity indicates either a too low concentrated sample or the absence of significant amount of colloidal structures within solution. It also renders the treatment of auto-correlation function more risky as the level of relative noise is dramatically increased.

In the case of *polydisperse and non-interacting nanoparticles,* the auto-correlation intensity function G(τ,q) no longer follows a single exponential decay but should be based on a sum or an integral over a distribution F(Γ) of the diffusion coefficient:

$$G(\tau,q) = A.(1+\beta.[\int_0^\infty F(\Gamma).e^{-\Gamma.\tau}\ d\Gamma\,]^2) \quad \text{with} \quad \int_0^\infty F(\Gamma)\ d\Gamma = 1 \qquad \textbf{(5)}$$

Note that this distribution is over the decay rate not over the size of particles.
The main difficulty is now to extract from the experimental autocorrelation function, the distribution function F(Γ). Two approaches can be used:

- if the distribution function is monomodal and narrow enough, one can use the cumulant analysis leading to the **Z-average diameter** and an estimate of the width of the distribution (**Polydispersity index PDI**).

- in the general case, one can estimate the distribution function by a discrete function. Fitting this function with the auto-correlation one will lead to a plot of the relative intensity of light scattered by particles in various size classes (**intensity size distribution**).

Determination of polydispersity by cumulant analysis. Using Taylor expansion and cumulants of the distribution function, one can demonstrate that the equation (5) leads to (Applied Optics 40(24) 4087 (2001):

$$G(\tau,q) = A(1+\beta.e^{-2\bar{D}.q^2\tau}.\left(1+\frac{\mu_2}{2!}.\tau^2-\frac{\mu_3}{3!}.\tau^3\ldots\right)^2) \qquad \textbf{(6)}$$

with $\overline{D}$ the average hydrodynamic diffusion coefficient,
μ_i the i th moment of the distribution function F defined as:
$\mu_i = \int_0^\infty F(\Gamma).(\Gamma - q^2.\overline{D})^i.d(\Gamma)$.

Fitting the experimental auto-correlation to the equation (6) by the least squares method gives easily:

- the average hydrodynamic diffusion coefficient which corresponds to the mean of the distribution F(Γ), assuming a single peak Gaussian distribution. The equivalent hydrodynamical diameter (through the Stokes Einstein equation, with the hypothesis that the nanoparticle are spherical – i.e. micelles, vesicles, polymersomes etc…-) can then be calculated and is called the intensity weighted **Z-average mean diameter.** The Z-average mean diameter is the recommended value to be used in quality control (ISO standard document 13321:1996 E and 22412). If the sample is not a solution of monomodal, spherical and monodisperse nanoparticle, the Z-average size can only be used to compare various samples measured in the same dispersant and same conditions.
- the value second moment (μ_2) leads to the **polydispersity index** corresponding to the relative standard deviation of that distribution (PdI). In the case of a Gaussian distribution, this is directly the variance of the distribution. If estimated, the third moment (μ_3) provides a measure of the skewness or asymmetry of the distribution.

Fit of the correlation function by multiple exponential: intensity size distribution. For *samples with a multiple size distribution*, G(τ,q) is written as a discreet sum of exponential functions:

$$G(\tau,q) = A.(1+\beta.[\sum_i\ \alpha_i.e^{-\Gamma_i.\tau}\ d\Gamma\,]^2) \qquad \textbf{(7)}$$

with α_i the intensity-weighted contribution of the Γ_i decay rate associated to particles having a diffusion coefficient of $D_i = \frac{\Gamma_i}{q^2}$. The intensity-weighted distribution is obtained from a deconvolution of the measured intensity autocorrelation function of the sample. Generally, this is accomplished by using a non-negatively constrained least squares (NNLS) fitting algorithm, common examples being CONTIN, General Purpose and Multiple Narrow Mode algorithms using a certain number of defined size classes. These different algorithms differed from each other by the level of noise which is kept before deconvolution process (also called regularization). Indeed, a small amount of noise in the correlation function can generate a large number of distributions. In the case of spherical homogeneous particles, the intensity-weighted particle size distribution is then obtained by using Stokes Einstein equation (3).

From intensity distribution to volume or number size distribution. The intensity distribution is naturally weighted according to the scattering intensity of each particle fraction or family. As such, the intensity distribution can be somewhat misleading, in that a small amount of aggregation or presence or a larger particle species can dominate the distribution. This distribution can be converted, using Mie theory, to a number distribution describing the relative proportion of multiple components in the sample based on their number rather than based on their scattering. Given the optical properties of the particle and the scattering angle, Mie theory estimates the scattering intensity M(x) as a function of particle diameter x, dispersant and particle optical properties. The discreet list of Γ_i decay rate associated weighted by α_i could be transformed into a list of radii R_i (assuming spherical particles) through the equation $D_i = \frac{\Gamma_i}{q^2} = k_B T/(6\pi\eta R_i)$ weighted by the coefficient $\alpha_i/M(R_i)$.

Alternatively, conversion can be roughly obtained by assuming that M(x) is proportional to R^6 (in the case of small homogeneous spheres – i.e. micelles but not vesicles or polymersomes -) which is only correct for particle below ca 100 nm of diameter. For vesicles or polymersomes, one may suppose that M(x) is proportional to $R^4.t^2$ where t is the thickness of the shell thickness (JICS 165, 512 (1994)). Note that the Mie theory implies that a particular model has been chosen to describe the particles (homogeneous, spheres, hollow spheres, coated spheres…).

When transforming an intensity distribution to a number distribution, different assumptions are used: *all particles are homogeneous and spherical*, *the optical properties of the particles are known and intensity distribution is correct*. Moreover DLS technique itself produces distributions with inherent peak broadening, so there will always be some error in the representation of the intensity distribution. As such, number distributions derived from these intensity distributions emphasizes information obtained from a small fraction of the collected data. Therefore they are best used for comparative purposes, or for estimating the relative proportions where there are multiple modes, or peaks, and should never be considered as absolute.

Figure S6B. DLS correlogram of $GdPO_4$/HyPAM and functionalized HyPAMs with NaCl

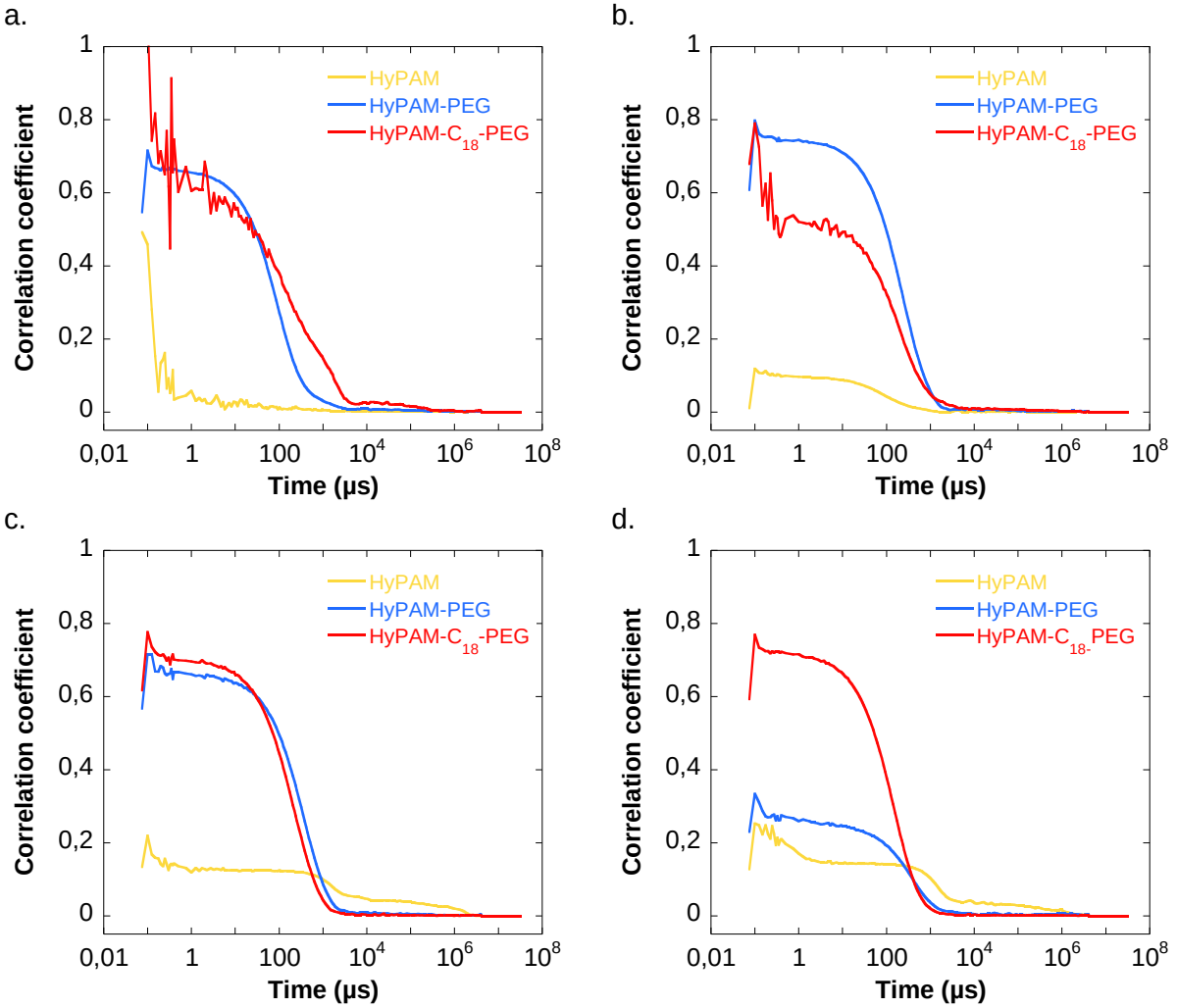

Figure S6B. Correlogram of $GdPO_4$/HyPAM and functionalized HyPAM for [NaCl]= a. 0M, b. 0.01M, c. 0.1M, d. 1M. [HyPAM]= 5 µmol.L^{-1}. The correlograms presented are the one obtained after filtration with a 0.45 micrometer cut-off filter, in the case of HyPAM these correlograms suggest that hybrids were retained at least partially within the filter. Therefore for HyPAM size were deduced from solution before filtration (See Figure S6A).

$GdPO_4$/HyPAM-core nanowires correlogram were found to exhibit aggregation process along with the addition of NaCl, whereas $GdPO_4$/PEG functionalized core-shell(s) correlogram remains well-defined up to 1 M NaCl added. These results highlight a high stability against ionic strength for pegylated hybrid systems.
Additional stability experiments were performed with HYPAM-C18-PEG (which seems to us the most promising system for in vivo experiments) in presence of albumin serum. No apparent modification of apparent hydrodynamic diameter of coated GdP NPs was observed after one week experiment and with no apparent modification of NPs morphology from TEM measurements.

S7. $GdPO_4$ / HyPAM, HyPAM-PEG, HyPAM-C_{18}-PEG – Drug loading capacity

Nile Red probe were used to examine the drug-loading capacity of these hybrids systems. This fluorescent probe is well-known to perform such studies[3–5] and is characterized by is solvatochromy (change of maximum emission wavelength according to the polarity of its surroundings).

Figure S7. Fluorescence studies of Nile Red in $GdPO_4$/HyPAM and functionalized HyPAMs systems

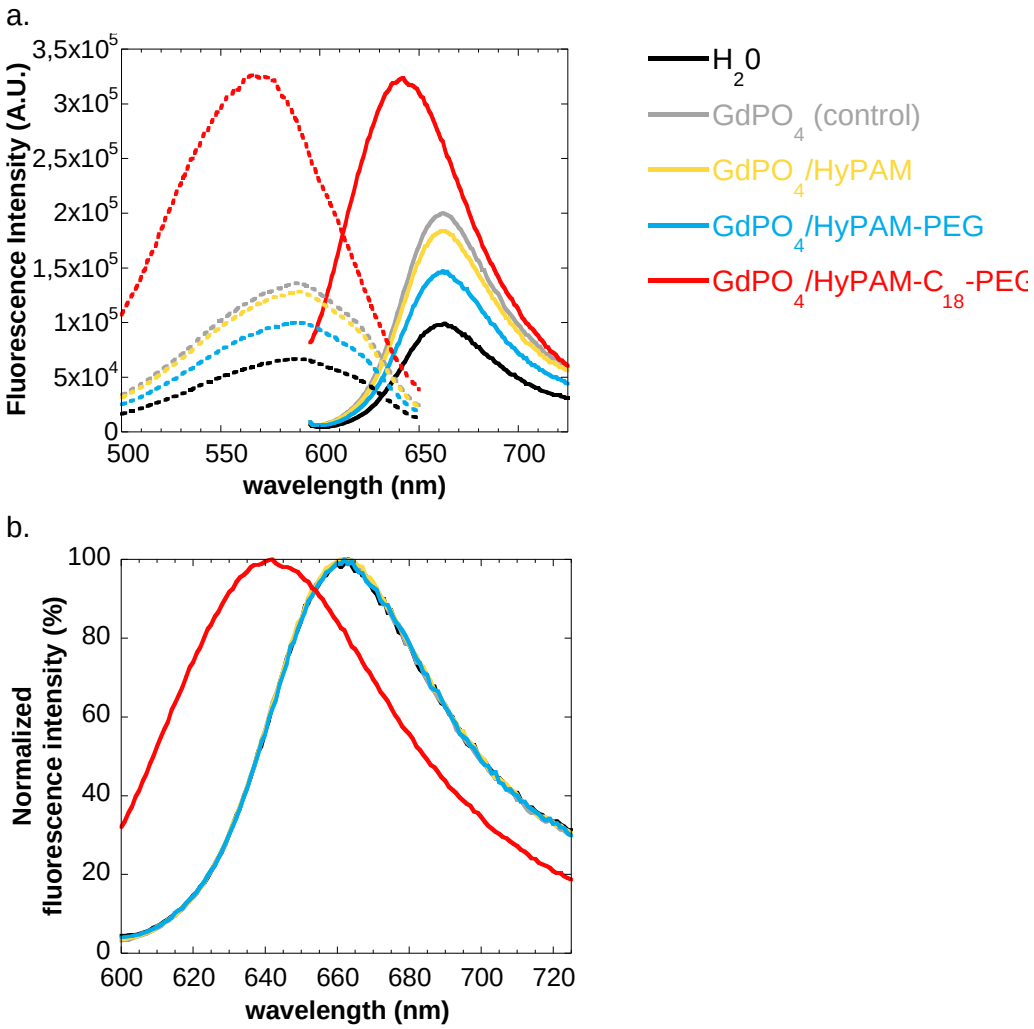

Figure S7A. a. excitation (dashed lines) and emission (solid lines) fluorescence intensity, b. normalized emission fluorescence intensity of 0.5µM Nile Red in H_20 (black), $GdPO_4$ (grey), $GdPO_4$/HyPAM (yellow), $GdPO_4$/HyPAM-PEG (blue) and $GdPO_4$/HyPAM-C_{18}-PEG with [Polymer]=1µM. λ_{ex}=590nm ; λ_{em}=660nm.

Nile Red added in H_2O, $GdPO_4$, $GdPO_4$/HyPAM and HyPAM-PEG systems does not show any change of maximum emission wavelength ($\lambda_{ex,max}$=662nm).
Nile Red in $GdPO_4$/HyPAM-C_{18}-PEG systems exhibit though a shift of maximum emission wavelength ($\lambda_{ex,max}$=642nm) corresponding to a dielectric constant about ε = 30 which is consistent with the presence of an apolar C_{18} layer in the core-shells HyPAM structure. This result highlight a drug-loading capacity of the $GdPO_4$/HyPAM-C_{18}-PEG .

S8. Cell viability of CEM cells in presence of GdPO4/HyPAM-C_{18}-PEG nanoparticles

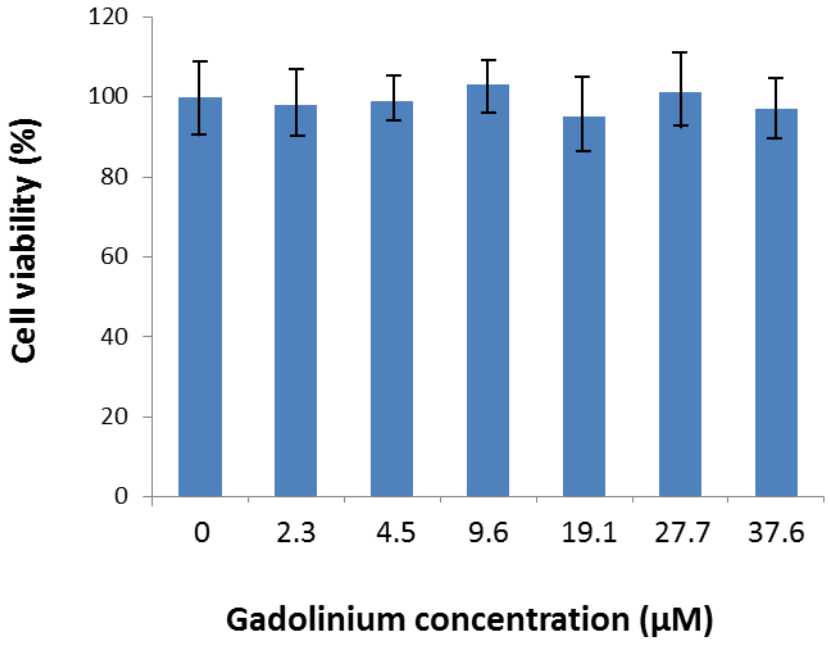

Figure S8. Cell viability of CEM cells in presence of GdPO4/HyPAM-C_{18}-PEG nanoparticles at different concentrations.

A. References

(1) Pérignon, N.; Mingotaud, A.; Marty, J.; Rico-lattes, I.; Mingotaud, C. *Chem. Mater.* **2004**, *16*, 4856–4858.

(2) Perignon, N.; Marty, J.; Dumont, M.; Rico-lattes, I.; Mingotaud, C. *Macromolecules* **2007**, *10*, 3034–3041.

(3) Greenspan, P.; Fowler, S. D. *J. Lipid Res.* **1985**, *26*, 781–789.

(4) Sackett, D. L.; Wolff, J. *Anal. Biochem.* **1987**, *167*, 228–234.

(5) Behnke, T.; Würth, C.; Hoffmann, K.; Hübner, M.; Panne, U.; Resch-Genger, U. *J. Fluoresc.* **2011**, *21*, 937–944.